

Theory of electronic Raman scattering in nearly antiferromagnetic Fermi liquids

T. P. Devereaux

Department of Physics, George Washington University, Washington, DC 20052

A. P. Kampf

Theoretische Physik III, Elektronische Korrelationen und Magnetismus, Institut für Physik, Universität Augsburg, D-86135 Augsburg, Germany

(Received 3 April 1998)

A theory of electronic Raman scattering in nearly antiferromagnetic Fermi liquids is constructed using the phenomenological electron-electron interaction introduced by Millis, Monien, and Pines. The role of ‘‘hot spots’’ and their resulting signatures in the channel dependent Raman spectra is highlighted, and different scaling regimes are addressed. The effects of self-consistency and vertex corrections are compared to a perturbative treatment of the interaction. The theory is then compared to Raman spectra taken in the normal state of cuprate superconductors, and it is shown that many features of the symmetry-dependent spectra can be explained by the theory. Remaining questions are addressed. [S0163-1829(99)04109-0]

I. INTRODUCTION

Recent results from angle resolved photoemission (ARPES) studies have shown that the planar quasiparticle (QP) dynamics in the normal state of high-temperature superconductors are extremely anisotropic.¹ For optimally doped samples with the highest T_c 's, the QP spectral function observed for Fermi surface crossings along the $(\pi,0)$ - (π,π) direction in the Brillouin zone (BZ) is smeared by strong scattering compared to the observed spectrum along the $(0,0)$ - (π,π) direction. This anisotropy becomes more pronounced as the materials are further underdoped with concomitantly lower transition temperatures into the superconducting state.² These effects have been ascribed to a strongly momentum-dependent QP self-energy $\Sigma(\mathbf{k},\omega)$ whose imaginary part is largest for \mathbf{k} near the BZ axes and yields a broadly incoherent spectral function. Understanding the nature and origin of this anisotropy could lead to a better understanding of the complex dynamics which cause the normal state of the cuprates to be very far away from being ‘‘normal.’’

Many theoretical efforts have been conducted to understand this planar anisotropy by calculating $\Sigma(\mathbf{k},\omega)$ for various types of interactions and via several methods. These efforts usually have focused on understanding the results from photoemission. Since ARPES is a single particle probe, the spectral function can be compared directly with experiment and provides direct contact to the self-energy around the BZ. However, most other probes (e.g., penetration depth, conductivity, tunneling density of states, etc.) involve averages around the BZ and thus are not so sensitive to the effects of anisotropic self-energies. Electronic Raman scattering is an exception. As demonstrated in the superconducting state,³ electronic Raman scattering is a two particle probe which has proven to be a useful tool to understand QP dynamics on selected regions of the BZ. The matrix elements for Raman scattering can be tuned by orienting incoming and outgoing photon polarizations, thereby projecting out different regions of the Fermi surface. In Ref. 3 it was shown how this tuning

could be used to provide a detailed probe of the momentum dependence of the superconducting energy gap.

In this regard, Raman scattering can be considered a complementary probe to ARPES. Raman measurements on several systems have shown a remarkable *channel* dependence in the normal state for the optimally and underdoped cuprates in a variety of systems.⁴⁻⁸ For scattering geometries of B_{1g} symmetry, an almost⁸ temperature-independent Raman spectrum has been observed up to frequencies of a few J , while for B_{2g} orientations the spectra show a temperature dependence that tracks that of the dc resistivity.^{5,7} Moreover, the overall magnitude of the electronic continuum is observed to be relatively independent of doping for the B_{2g} channel, but decreases dramatically with underdoping for the B_{1g} channel, with spectral weight transferring out to two-magnon energies.^{7,8} One is to conclude that the QP's near $(\pi,0)$ which are probed by the B_{1g} channel are particularly incoherent and become more incoherent with underdoping, in agreement with the results from ARPES. Coupled to the flatness of the bands there, these QP's are likely not to participate in transport.⁹ Currently there is no theoretical understanding of Raman scattering in the normal state of the cuprates, as all previous theories failed to predict large differences between these two channels at low frequencies. This is due to the neglect of strongly anisotropic electron interactions. It is the purpose of this paper to address these issues.

It is widely believed that strong antiferromagnetic (AF) correlations are an important ingredient needed to describe the unusual properties found in the normal state of the cuprate superconductors and provides the origin of the strongly anisotropic dynamics in the cuprates. Large QP scattering for momentum transfers near the AF wave vector $\mathbf{Q} = (\pi/a, \pi/a)$ have been invoked to explain the photoemission results.^{10,11} Therefore we have studied the phenomenological nearly antiferromagnetic Fermi liquid (NAFL) model¹² as an example of highly anisotropic scattering to investigate the two-particle Raman response. The NAFL model has at its center a strong magnetic interaction between

planar QP's which is peaked at or near \mathbf{Q} and yields anisotropic self-energies. This model has been widely applied to investigate both spin and charge properties.^{13,14} Our results show that the Raman response is an ideal probe to clarify the nature of QP dynamics on regions of the Fermi surface.

The outline of the paper is as follows. Section II reviews and outlines a generalized approach to calculate nonresonant Raman scattering in correlated electron systems and introduces the model interaction. Section III investigates the NAFL model using simple perturbation theory. The scattering rate for QP's on different regions of the Fermi surface is calculated and the subsequent Raman response is obtained. Section IV compares the results of the calculations in Sec. III to data on overdoped $\text{Bi}_2\text{Sr}_2\text{CaCu}_2\text{O}_{8+\delta}$ (Bi-2212). Section V investigates the role of a self-consistent treatment of the interaction and the role of vertex corrections. Finally Sec. VI summarizes our results and states our conclusions.

II. FORMALISM

The intensity of inelastically scattered light can be written in terms of a differential photon scattering cross section as

$$\frac{\partial^2 \sigma}{\partial \omega \partial \Omega} = \frac{\omega_S}{\omega_I} r_0^2 S_{\gamma\gamma}(\mathbf{q}, \omega),$$

$$S_{\gamma\gamma}(\mathbf{q}, \omega) = -\frac{1}{\pi} [1 + n(\omega)] \text{Im} \chi_{\gamma\gamma}(\mathbf{q}, \omega). \quad (1)$$

Here $r_0 = e^2/mc^2$ is the Thompson radius, ω_I, ω_S are the frequency of the incoming and scattered photon, respectively, and we have set $\hbar = k_B = 1$. $S_{\gamma\gamma}$ is the generalized structure function, which is related to the imaginary part to the Raman response function $\chi_{\gamma\gamma}$ through the fluctuation-dissipation theorem, the second part of Eq. (1). $n(\omega)$ is the Bose-Einstein distribution function. The Raman response measures ‘‘effective density’’ fluctuations

$$\chi_{\gamma\gamma}(i\omega) = \int_0^{1/T} d\tau e^{-i\omega\tau} \langle T_\tau [\tilde{\rho}(\tau) \tilde{\rho}(0)] \rangle, \quad (2)$$

with T_τ the time-ordering operator and the imaginary part is obtained by analytic continuation $i\omega \rightarrow \omega + i0^+$.

The Raman intensity can be represented as a scattering off an effective charge density¹⁵

$$\tilde{\rho} = \sum_{\mathbf{k}, \sigma} \gamma(\mathbf{k}; \omega_I, \omega_S) c_\sigma^\dagger(\mathbf{k}) c_\sigma(\mathbf{k}), \quad (3)$$

where σ is the spin index and $\gamma(\mathbf{k}; \omega_I, \omega_S)$ is the Raman scattering amplitude. The effective charge density is a non-conserving quantity in contrast to the real charge.¹⁶ Here the Raman vertices γ are related to the incident and scattering photon polarization vectors $\mathbf{e}^{I,S}$, resulting from a coupling of both the charge current and the charge density to the vector potential. In general the Raman vertex depends nontrivially on both the incident and scattered photon frequencies. According to Abrikosov and Genkin,¹⁷ if the energies of the incident and scattered frequencies ω_I, ω_S are negligible compared to the energy band gap, γ can be expressed in terms of the curvature of the bands and the incident and scattered photon polarization vectors $\mathbf{e}^{I,S}$ as

$$\lim_{\omega_I, \omega_S \rightarrow 0} \gamma(\mathbf{k}; \omega_I, \omega_S) = \sum_{\mu, \nu} e_\mu^I \frac{\partial^2 \epsilon(\mathbf{k})}{\partial k_\mu \partial k_\nu} e_\nu^S, \quad (4)$$

where terms of the order of $1 - \omega_S/\omega_I$ are dropped. This expression is valid if the incoming laser light cannot excite direct band-band transitions. However, one might question the appropriateness of this approximation for the cuprates given that typical incoming laser frequencies are on the order of 2 eV.

An alternative approach is based on the experimental observation that the electronic continua in the metallic normal state for a wide range of cuprate materials depend only mildly on the incoming laser frequency. Since the polarization orientations transform as various elements of the point group of the crystal, one can use symmetry to classify the scattering amplitude, viz.,

$$\gamma(\mathbf{k}; \omega_I, \omega_S) = \sum_L \gamma_L(\omega_I, \omega_S) \Phi_L(\mathbf{k}), \quad (5)$$

where $\Phi_L(\mathbf{k})$ are either Brillouin zone (BZH, orthogonal over the entire Brillouin zone) or Fermi surface (FSH, orthogonal on the Fermi surface only) harmonics which transform according to point group transformations of the crystal.¹⁸ Representing the magnitude but not the \mathbf{k} dependence of scattering, the prefactors can be approximated to be frequency independent and taken as model constants to fit absolute intensities.

Thus we have simplified the many-band problem in terms of symmetry components which can be related to charge degrees of freedom over portions of the BZ. While sacrificing information pertaining to overall intensities, we have gained the ability to probe and compare excitations on different regions of the BZ based solely on symmetry classifications. This can be illustrated by considering the various experimentally accessible polarization orientations.

Using an x, y coordinate system locked to the CuO_2 planes, incident and scattered light polarizations aligned along $\hat{x} + \hat{y}, \hat{x} - \hat{y}$, for example, transform according to B_{1g} symmetry, and thus

$$\Phi_{B_{1g}}(\mathbf{k}) = \cos(k_x a) - \cos(k_y a) + \dots, \quad (6)$$

where the ellipses are higher order BZH. Likewise, $\mathbf{e}^{I,S}$ aligned along \hat{x}, \hat{y} transforms as B_{2g} :

$$\Phi_{B_{2g}}(\mathbf{k}) = \sin(k_x a) \sin(k_y a) + \dots \quad (7)$$

The A_{1g} basis function is

$$\begin{aligned} \Phi_{A_{1g}}(\mathbf{k}) = & a_0 + a_2 [\cos(k_x a) + \cos(k_y a)] \\ & + a_4 \cos(k_x a) \cos(k_y a) \\ & + a_6 [\cos(2k_x a) + \cos(2k_y a)] + \dots, \end{aligned} \quad (8)$$

with the expansion parameters a_i determined via a fitting procedure with experiment. The A_{1g} response is not directly

accessible from experiments and must be obtained by subtracting several combinations of the response for various polarization orientations.

By considering the \mathbf{k} dependence of the basis functions, it is clear that the B_{1g} part of the spectra probes light scattering events along the k_x or k_y axes, B_{2g} probes the diagonals, and A_{1g} is a weighted average over the entire Brillouin zone. In this manner information about the momentum dependence of the QP scattering rate can be obtained. Since we are interested in probing anisotropy effects we will focus on B_{1g} and B_{2g} and not consider the A_{1g} channel.

Since the momentum transfer by the photon is negligible compared to the momentum of the electrons in metals, we are interested in the $\mathbf{q}=0$ Raman response. With the approximations above, the gauge invariant Raman response is of the form

$$\chi_{\gamma\gamma}(\mathbf{q}=0, i\Omega) = -\frac{T}{N} \sum_{i\omega} \sum_{\mathbf{k}} \gamma(\mathbf{k}) G(\mathbf{k}, i\omega) \times G(\mathbf{k}, i\omega + i\Omega) \tilde{\gamma}(\mathbf{k}, i\omega, i\omega + i\Omega), \quad (9)$$

with the renormalized vertex $\tilde{\gamma}$ obeying a Bethe-Salpeter equation

$$\tilde{\gamma}(\mathbf{k}, i\omega, i\omega + i\Omega) = \gamma(\mathbf{k}) + \frac{T}{N} \sum_{i\omega'} \sum_{\mathbf{k}'} \times V(\mathbf{k}-\mathbf{k}', i\omega - i\omega') G(\mathbf{k}', i\omega') \times G(\mathbf{k}', i\omega' + i\Omega) \tilde{\gamma}(\mathbf{k}', i\omega', i\omega' + i\Omega). \quad (10)$$

Here V is the effective QP interaction in the particle-hole channel to be discussed below, and N is the number of sites. In the absence of vertex corrections to the Raman vertex $\gamma(\mathbf{k})$, the Raman response is given by

$$\chi''_{\gamma\gamma}(\mathbf{q}=0, \Omega) = \frac{2}{N} \sum_{\mathbf{k}} \gamma^2(\mathbf{k}) \int \frac{d\omega}{\pi} \times [f(\omega) - f(\omega + \Omega)] G''(\mathbf{k}, \omega) \times G''(\mathbf{k}, \omega + \Omega). \quad (11)$$

The Green's function is given in terms of the self-energy Σ by Dyson's equation, $G(\mathbf{k}, \omega) = [\omega - \varepsilon(\mathbf{k}) - \Sigma(\mathbf{k}, \omega)]^{-1}$. We use a two-dimensional (2D) tight binding band structure $\varepsilon(\mathbf{k}) = -2t[\cos(k_x a) + \cos(k_y a)] + 4t' \cos(k_x a) \cos(k_y a) - \mu$, and from now on we set the lattice constant $a=1$.

III. PERTURBATION THEORY AND ROLE OF SCATTERING

A. Other models

Before we introduce the NAFL portion of the calculation, we start by considering the simple form for the Raman response given in Eq. (11). We first consider noninteracting electrons. In that case, the imaginary part of the Green's functions are simply δ functions, and thus the $q \rightarrow 0$ Raman response is given essentially by the Lindhard function weighted by the Raman vertex. Since for $q=0$ there is no

phase space available to create electron-hole pairs at low energies, this limit would yield no Raman cross section. Thereby, it is crucial to have a nonzero self-energy in order to observe inelastic light scattering at all in this limit.

Zawadowski and Cardona considered free electrons in the presence of a potential due to impurities.¹⁹ Using Eqs. (9) and (10) and assuming mainly isotropic impurity scattering, $\Sigma(\mathbf{k}, \omega) = -i/\tau_{L=0}$, as well as a separable interaction diagonal in Fermi surface harmonics $\phi_L, V(\mathbf{k}-\mathbf{k}') = V_{\mathbf{k},\mathbf{k}'} = \sum_L V_{LL} \phi_L(\mathbf{k}) \phi_L^*(\mathbf{k}')$, the resulting cross section can be written in a Lorentzian form,

$$\chi''_{LL}(\Omega) = 2N_F \gamma_L^2 \frac{\Omega \tau_L^*}{1 + (\Omega \tau_L^*)^2}, \quad (12)$$

where a flat band with density of states per spin at the Fermi level N_F has been assumed, and $1/\tau_L^* = 1/\tau_{L=0} - 1/\tau_L$ is the impurity scattering rate in channel L reduced by vertex corrections. Finally γ_L is the prefactor of the Raman vertex in channel L [see Eq. (5)]. While impurities do yield a channel dependent response if the V_{LL} are different for different L , since the spectra have a peak at the scattering rate and then fall off at large ω , it cannot fit the large flat continuum observed in Raman experiments extending up to the scale of a few eV.⁴⁻⁸

A form similar to Eq. (12) has been obtained for the case of QP scattering in a nested Fermi liquid.²⁰ The calculated spectra have the same form as Eq. (12) except that a frequency- and temperature-dependent scattering rate is introduced which is of the form $1/\tau_L^* = \max\{\beta_L T, \alpha_L \omega\}$, with channel-dependent prefactors β, α . This form for the response gives qualitatively good agreement with the observed spectra,²⁰ but does not yield appreciably large differences between response functions for different channels. In principle features of the QP interaction due to nesting, which is pronounced for particular momentum transfers near the nesting wave vector, may well account for the observed scattering anisotropy. However, calculations have not been performed for model Fermi surfaces.

B. NAFL theory

Therefore, we now consider a form for the QP interaction due to an effective spin-fermion model interaction¹²

$$V(\mathbf{q}, \Omega) = g^2 \frac{\alpha \xi^2}{1 + (\mathbf{q}-\mathbf{Q})^2 \xi^2 - i\Omega/\omega_{sf}}. \quad (13)$$

This interaction forms the basis of the NAFL theory, and has been derived by considering the interaction of electrons to external spin degrees of freedom^{21,13} and describes at low temperatures and several dopings the effective interaction calculated via FLEX (Ref. 11) and quantum Monte Carlo²² treatments of the 2D Hubbard model. Recently the optical conductivity was explored within this model and was found to be in relatively good agreement with experiments.¹⁴ Our efforts complement this study and investigate the consequences of Eq. (13) in greater detail.

The self-energy at lowest order is given by

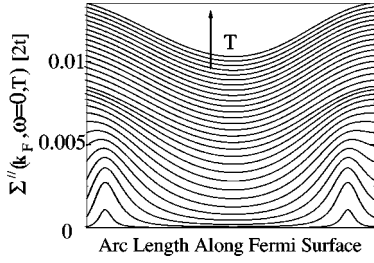


FIG. 1. Quasiparticle scattering rate around a section of the Fermi surface for different temperatures in the NAFL model. Here we have taken $\omega_{sf}/2t = 0.00876 + 6.14T/2t$ for all T and $\omega_{sf}\xi/2t = 0.1058$ for $T/2t < 0.0273$ ($z=1$), and then taken $\omega_{sf}\xi^2/2t = 0.0635$ for $0.6 > T/2t > 0.0273$ ($z=2$).

$$\Sigma(\mathbf{k}, i\omega) = -\frac{T}{N} \sum_{i\omega'} \sum_{\mathbf{p}} V(\mathbf{k}-\mathbf{p}, i\omega-i\omega') G(\mathbf{p}, i\omega'), \quad (14)$$

with G the single particle Green's function. Here ω_{sf} and ξ are the phenomenological temperature-dependent spin fluctuation energy scale and the correlation length, respectively, which have been determined via fits to magnetic response data.¹³ For optimally doped and underdoped systems, the strong AF correlations produce three magnetic regions in the normal state. In the phase diagram constructed in Ref. 13, ω_{sf} and ξ obey certain relations depending on temperature and doping regimes. For each scaling regime, $\omega_{sf}\xi^z = \text{constant}$ (i.e., temperature independent), with z the dynamical critical exponent. For the $z=2$ regime the spin correlations are governed by temperature driven fluctuations at a temperature above T_{cr} . As the temperature is reduced below T_{cr} the $z=1$ or pseudoscaling regime is reached where the spin correlations are strong enough to lead to changes from the classical mean field $z=2$ regime. T_{cr} is taken to be doping dependent and rises with underdoping. Therefore the $z=1$ region plays a more dominant role in the phase diagram than $z=2$ for underdoped systems while for appreciably overdoped systems, the $z=1$ region vanishes. At lower temperatures still and away from overdoped systems a crossover to a pseudogap state occurs at T^* . However, we will not concentrate on this region and defer a discussion of pseudogap effects to the last section.

As in Ref. 14, we use the following approximations: (i) we neglect the real part of the self-energy, (ii) evaluate the Green's function at lowest order in the coupling constant g^2 , (iii) neglect all vertex corrections for the Raman vertex, and (iv) momentum sums are replaced by $\sum_{\mathbf{k}} = \int d(\Omega_{\mathbf{k}}/|\mathbf{v}_{\mathbf{k}}|) \int d\varepsilon(\mathbf{k})$. While (iv) does not crucially affect the results, approximations (i)–(iii)—while simplifying the calculations—considerably miss important QP renormalizations at larger values of the coupling. Therefore we expect that these calculations would be most appropriate to describe the spectra taken on overdoped cuprate superconductors.

1. Quasiparticle scattering rate

We first start by consider the effective QP scattering rate around the Fermi surface. In Fig. 1 we show the QP scattering rate, defined as the imaginary part of the self-energy $\Sigma(\mathbf{k}, \omega=0, T)$, around the Fermi surface as a function of temperature T . Here the effective coupling constant is taken

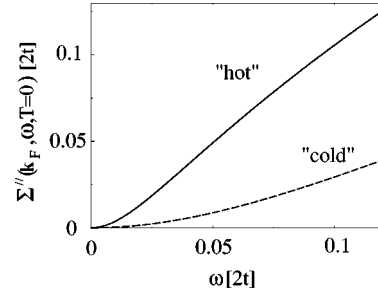


FIG. 2. Quasiparticle scattering rate for ‘‘hot’’ and ‘‘cold’’ spots on the Fermi surface as a function of frequency for $T=0$. The ‘‘hot’’ spot corresponds to $\mathbf{k}_F=(3.026, 0.4817)$ while the ‘‘cold’’ spot corresponds to $\mathbf{k}_F=(1.107, 1.107)$. Here the $z=1$ parameters as given in the caption of in Fig. 1 are used.

as $\alpha g^2/2t = 6.25$. As a result of our perturbative approach, the magnitude of the scattering rate scales directly with αg^2 . The band structure parameters are chosen to be most applicable to slightly overdoped systems: $t'/t = 0.45$ and a filling $\langle n \rangle = 0.8$. The other parameters of the theory are chosen to provide a smooth link from the $z=2$ to the $z=1$ scaling regimes, as defined in the figure caption.

Figure 1 shows that the scattering rate is extremely anisotropic around the Fermi surface, having ‘‘hot regions’’ (near the zone axes) where the QP scattering rate is peaked, and ‘‘cold regions’’ (near the zone diagonals) where the rate is smallest. The ‘‘hot spots’’ are those regions of the Fermi surface which can be connected by \mathbf{Q} . These regions are close to the zone axes for the given band structure, and the B_{1g} geometry most effectively probes these hot spots while the B_{2g} geometry probes along the zone diagonals and therefore sees ‘‘colder’’ QP's. The difference between the scattering at the ‘‘hot’’ and ‘‘cold’’ regions is smallest at high temperatures, and is due largely to the enhanced density of states near the zone axes. As the temperature cools the ‘‘hot spots’’ become more developed and more strongly peaked as the interaction becomes sharply peaked for momentum transfers near \mathbf{Q} .

Next we consider the frequency dependence of the scattering rate away from the Fermi level. This is shown in Fig. 2, where the QP scattering rate at $T=0$ is plotted for both ‘‘hot’’ and ‘‘cold’’ QP's, as defined in the figure caption. Both scattering rates vary as ω^2 at small ω , characteristic of a Fermi liquid, but cross over to a behavior which is effectively linear in ω at larger frequencies. For the ‘‘hot’’ QP's this crossover happens at smaller values of ω (0.025, in units of $2t$) than for the ‘‘cold’’ QP's (0.092). Moreover, the scattering is once again larger for the ‘‘hot’’ spots than for the ‘‘cold.’’ Similar results have been obtained in Refs. 14, 13, and the reader is directed to that reference for further details. From the point of view of Raman scattering, we would expect that the different magnitude and frequency and temperature dependence of the scattering rate around the Fermi surface will be manifest in the channel-dependent Raman response.

2. Channel-dependent Raman response

Considering the Raman response, we see that the B_{1g} part of the spectra probes the ‘‘hot regions’’ of large QP scatter-

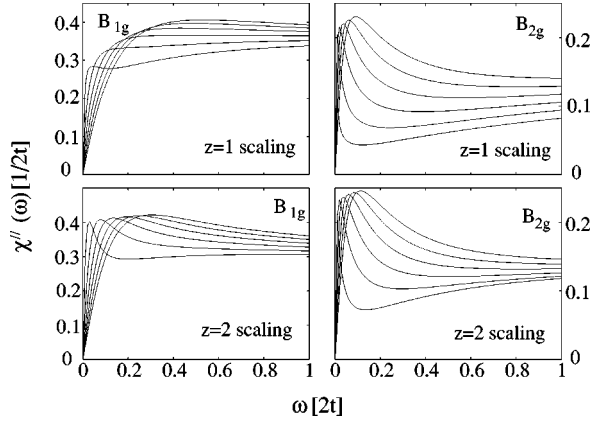


FIG. 3. Electronic Raman response for the B_{1g} and B_{2g} channels evaluated at different temperatures ($T/2t = 0.01, 0.02, \dots, 0.06$ from top to bottom) for the $z=1$ and the $z=2$ scaling regimes of NAFL theory. Here we have set $b_1 = b_2 = 1$, as defined in the text.

ing while B_{2g} probes the ‘‘cold regions.’’ This means that the B_{1g} response should probe less coherent QP’s than the B_{2g} response, which should be reflected in the temperature dependence and general line shape of the Raman continuum.

Within our perturbative approach we present in Fig. 3 the results for the B_{1g} and B_{2g} Raman response functions for both $z=1$ and $z=2$ scaling regimes. The parameters we have used for both scaling regimes are $g=1$ eV, $\alpha=3.1$ states/eV, $t=250$ meV, $t'/t=0.45$, filling $\langle n \rangle = 0.8$, $\gamma_{B_{1g}}(\mathbf{k}) = b_1 [\cos(k_x) - \cos(k_y)]$, $\gamma_{B_{2g}}(\mathbf{k}) = b_2 \sin(k_x) \sin(k_y)$. In addition, for the $z=1$ scaling regime we have used $\omega_{sf} \xi = 50$ meV and $\xi^{-1} = 0.1 + 4.64T/2t$, while for the $z=2$ scaling regime, $\omega_{sf} \xi^2 = 60$ meV and $\omega_{sf}/2t = 0.0237 + 0.55T/2t$. These parameters are similar to those used in Ref. 14 to describe the Hall conductivity data in $\text{YBa}_2\text{Cu}_3\text{O}_7$. Here the absolute magnitude for the scattering is arbitrary and determined by the dimensionless coefficients b_1 and b_2 , which are set by fitting to the data. This has no effect on the frequency-dependent line shapes.

The spectra for both scaling regimes share several features. First, the flat continuum at high frequencies which is present in the Raman data from all cuprate superconductors is reproduced by the theory. This is a consequence of a scattering rate $\Sigma''(\omega)$ which is effectively linearly dependent on ω at frequency scales larger than ω_{sf} , as shown in Fig. 2. The spectra rise linearly with ω with a smaller slope for large scattering than for weaker scattering. More importantly, the Raman response is different for the two scattering geometries as a consequence of the strong anisotropy of the scattering rate. This is due to the relative magnitude and frequency dependence of the scattering rate. As shown in Figs. 1 and 2, the scattering rate probed in the B_{1g} channel is larger than B_{2g} for all frequencies and temperatures and becomes effectively linear in frequency at a much smaller frequency than that probed by the B_{2g} channel. Thus the position of the peak of the spectra in the B_{1g} channel is at a larger frequency in all figures compared to the B_{2g} channel, and the B_{1g} spectra is overall flatter than the B_{2g} spectra.

The differences between the $z=1$ and $z=2$ results are largely quantitative but once again show the influence of the anisotropy of the QP scattering. The B_{1g} spectra show the

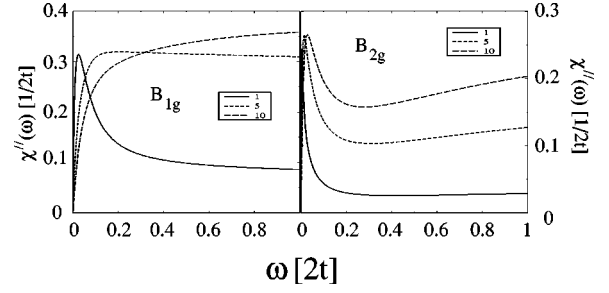


FIG. 4. The B_{1g} and B_{2g} Raman continua are plotted for $T/2t = 0.03$ for values of the effective coupling constant $g_{\text{eff}} = 1, 5, 10$, as defined in the text. The $z=1$ parameters were used for ω_{sf} and ξ as in Fig. 3.

greater difference between the two scaling regimes, as the overall spectra appears flatter for $z=1$ than for $z=2$. This is due to the more pronounced hot spots in the $z=1$ regime. The B_{1g} channel thus is more sensitive than the B_{2g} channel to the growth of the correlation length as temperature is lowered. Features of a crossover from $z=2$ to $z=1$ scaling as the temperature is lowered through T_{cr} would be most evident in the B_{1g} channel.²³

The role of the effective coupling constant is to determine the overall shape of the continuum due to the increase in the QP scattering rate. An increase of the coupling constant leads to (i) an increase in the overall magnitude of the cross section, (ii) flatter spectra, and (iii) the movement of the weak peak of the spectra out to larger energy scales. This is shown in Fig. 4 which plots the B_{1g} and B_{2g} response as a function of frequency shift at low temperatures $T/2t = 0.03$ for different values of $g_{\text{eff}} = \alpha g^2/2t$. As a consequence, the sensitivity of the Raman spectra to the details of the parameters can be a very useful tool to probe the anisotropic QP scattering rates in much the same way as it has been used to probe the anisotropy of the energy gap $\Delta(\mathbf{k})$ in the superconducting state.³

IV. FIT TO OVERDOPED Bi-2212

As we remarked, the approximations used [(i)–(iv) listed in Sec. III B] are most appropriate for systems with weak spin fluctuation scattering and therefore we expect that our results would best represent the data from appreciably overdoped cuprate superconductors. Before we consider the effects of a more consistent treatment of the interactions in NAFL beyond perturbation theory, it is useful to explore how the perturbative theory compares to the data on overdoped cuprates in their normal state.

For a comparison to these data we thus consider the results from the $z=2$ scaling regime in closer detail. Overdoped samples typically have higher residual resistivities than optimally doped samples. While this may be due in part to sample preparation, it is believed that the overdoped cuprates’ increased effective dimensionality allows the QP’s to interact more strongly with defects residing out of the CuO_2 planes.³ Therefore in addition we will consider an isotropic impurity interaction $H_{\text{imp}} = \sum_{\mathbf{k}, \mathbf{k}'} \sum_{i, \sigma} U e^{i(\mathbf{k}-\mathbf{k}') \cdot \mathbf{R}_i} c_{\mathbf{k}, \sigma}^\dagger c_{\mathbf{k}', \sigma}$, where \mathbf{R}_i denotes the position of the impurity labeled by i and U is the impurity potential. After averaging over the position of the impurities, this adds a momentum-

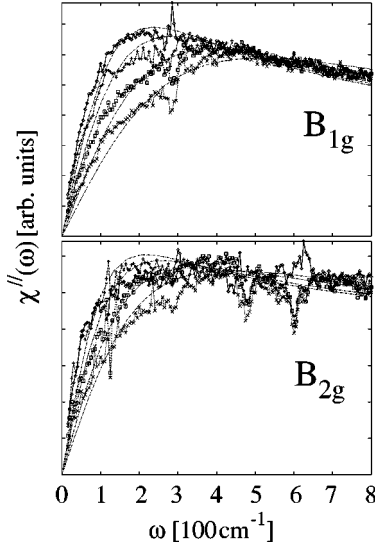


FIG. 5. Fit of the $z=2$ NAFL theory to the B_{1g} and B_{2g} spectra taken in Ref. 6 on appreciably overdoped $\text{Bi}_2\text{Sr}_2\text{CaCu}_2\text{O}_{8+\delta}$ ($T_c = 55$ K) at 60, 90, 150, and 200 K from top to bottom. Parameters used are given in the text.

independent term to the imaginary part of the self-energy $\Gamma_{\text{imp}} = \pi n_i N_F |U|^2$, where n_i is the impurity concentration and N_F is the density of states per spin at the Fermi level.

The fit of the theory to the temperature-dependent spectra for each channel obtained in appreciably overdoped Bi 2212 ($T_c = 55$ K) by Hackl *et al.* in Ref. 6 is shown in Fig. 5 for the B_{1g} and B_{2g} channels. The impurity scattering rate for this material can be estimated from the extrapolated $T=0$ dc resistivity of approximately $30 \mu\Omega \text{ cm}$.²⁴ Assuming a Drude resistivity and using a plasma frequency of 1.6 eV given in Ref. 24 yields $\Gamma_{\text{imp}} = 40 \text{ cm}^{-1}$. We note that ω_{sf} and ξ have so far not been determined via fits to magnetic response data. The fits are obtained by choosing: ω_{sf} and ξ at a fixed temperature, a magnitude of the coupling constant αg^2 , and lastly b_1 and b_2 . Then, only the temperature-dependent part of ω_{sf} was modified to fit the data at other temperatures. We have used $b_2/b_1 = 0.417$, $\omega_{sf}\xi^2 = 13 \text{ meV}$, and $\omega_{sf} = 160 \text{ K} + 0.06T$ [K]. This parameter choice leaks to remarkably good agreement with the data. The flatness of the continuum for both channels emerges from the theory and the relative peak positions come out correctly. More importantly, for the first time the temperature dependence of the spectra in both channels can be explained. NAFL provides an excellent description of the QP dynamics in the overdoped region.

Further information on QP dynamics can be obtained from the slope of the spectra at vanishing frequencies. We denote this slope as $\Gamma_\lambda = \lim_{\Omega \rightarrow 0} \Omega / \chi''_\lambda(\Omega)$, for $\lambda = B_{1g}$ or B_{2g} . In Ref. 6 it was shown that the inverse of this slope has qualitatively different behaviors for different doping regimes of various cuprate materials. While the inverse slope observed in the B_{2g} channel always was found to track the temperature dependence of the dc resistivity for all regions of doping, the B_{1g} inverse slope showed a remarkable sensitivity to doping. For overdoped systems, the B_{1g} slope was similar to the B_{2g} rate, and effectively followed the behavior $\Gamma_{B_{1g}} \sim \Gamma_{B_{2g}} \sim \text{const} + T^2$. For optimally doped cuprates,

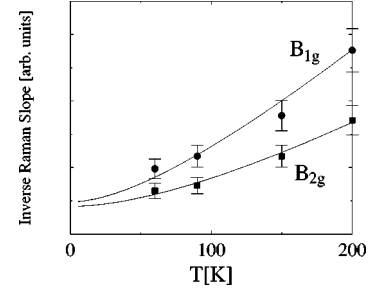


FIG. 6. Fit of the inverse slope of the Raman response for the two symmetry channels. The error bars are from Ref. 25.

$\Gamma_{B_{2g}} \sim T$, while $\Gamma_{B_{1g}} \sim \text{const}$. Moreover, for underdoped materials the B_{1g} inverse slope was found to increase with decreasing temperature, indicative of insulating behavior.

Within the level of our approximations, the low frequency Raman response is given by

$$\begin{aligned} 1/\Gamma_\gamma(T) &= \lim_{\Omega \rightarrow 0} \chi''_{\gamma\gamma}(\Omega)/\Omega \\ &= \int \frac{d\Omega_{\mathbf{k}}}{|\mathbf{v}_{\mathbf{k}}|} \gamma^2(\mathbf{k}) \int \frac{dx}{[2 \cosh(x/2)]^2} \frac{1}{\Sigma''(\mathbf{k}, xT)}. \end{aligned} \quad (15)$$

The inverse slope samples the QP scattering lifetime at regions of the Fermi surface selected by the light polarization orientations. It is important to note that in this level of approximation the momentum dependence of the Raman vertices competes with the momentum-dependent scattering rate on the Fermi surface since the largest contribution to the integral in Eq. (15) comes from where the Raman vertex is the largest and where the QP scattering rate is the smallest. Therefore, the Raman inverse slope washes out direct information about the k dependence of the scattering rate and leads to a more similar behavior of the B_{1g} and B_{2g} inverse slope, which hides the underlying anisotropy of the QP scattering rate. This is due to the approximations of restricting consideration to the Fermi surface only and to the neglect of vertex corrections. In the following section this is shown to be crucial if the spin fluctuations are strong.

However, for weak spin fluctuations, we believe that the data on overdoped materials can be best fit with this perturbative approach. In Fig. 6 we plot the inverse Raman slope obtained from the parameters used in Fig. 5 and compare the results to the data taken in Ref. 6. The agreement confirms the fits in Fig. 5. The data are consistent with a scattering rate which is not too anisotropic, and is governed by elastic scattering from impurities and Fermi liquid inelastic scattering from spin fluctuations. We remark that the fits are robust to small NAFL parameter changes.

V. SELF-CONSISTENCY AND VERTEX CORRECTIONS

While good agreement between the theory and the data has been shown for overdoped Bi 2212, several features remain to be explained in optimally and underdoped systems. As mentioned in the last section, the difference of the inverse slope of the Raman response between B_{1g} and B_{2g} channels grows remarkably upon lesser dopings.⁶ Moreover, features

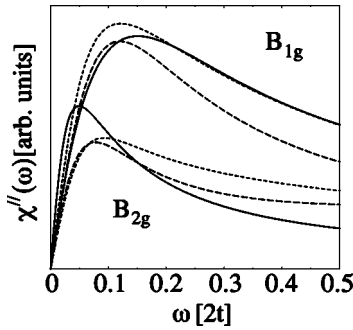


FIG. 7. Comparison of the $z=2$ (overdoped) results obtained from perturbation theory (solid line), self-consistent treatment (short dashed line), and the additional inclusion of vertex corrections (long dashed lines).

which have been associated with a pseudogap have been observed in the underdoped systems.^{7,8} Since our fits to the data were restricted by our approximations to weak spin fluctuations, we need an improved formalism for an insight into the effects of strong spin fluctuations.

Therefore for the remainder of the paper we solve the model lifting the restrictions (i)–(iv) listed before. The calculations were performed by first solving for the Green’s function Eq. (14) self-consistently while maintaining a filling $\langle n \rangle = 0.8$. We used a hard frequency cutoff $\omega^* = 0.4$ eV for the interaction Eq. (1) to improve convergence, but note that our results hardly were affected by this cutoff. Then the Bethe-Salpeter equation (10) was evaluated for the renormalized vertex. The calculations were carried out on the imaginary frequency axis using 256 Matsubara frequencies and 64×64 to 128×128 \mathbf{k} points. These values are similar to that used for resistivity studies.²⁶ The integral equation for the vertex $\tilde{\gamma}(\mathbf{k}, i\omega, i\omega + i\Omega)$ was solved for each external (internal) bosonic (fermionic) Matsubara frequency $i\Omega$ ($i\omega$). Once completed, the Raman response was evaluated using Eq. (9) and the results were analytically continued to the real frequency axis using Padé approximants.²⁷ Since the Raman response is in general quite featureless the Padé procedure was highly accurate (using 20–60 points changes the results by less than 5%).

We first consider how the perturbation results for the $z=2$ regime are affected. The results are summarized in Fig. 7 which compares the effects of self-consistency and vertex renormalizations to the results from perturbation theory for $T=0.08t$. ω_{sf} , ξ , and g_{eff} were chosen as in Fig. 3. By noting that the position of the peak in the B_{1g} channel decreases in frequency while the B_{2g} peak position increases under self-consistency, it can be seen that the effect of a self-consistent treatment is to decrease the relative anisotropy in the scattering rate around the Fermi surface leading to a more effectively “isotropic” response which places the peak of the spectra at nearly the same position ($\sim 0.2t$) for both channels. The B_{1g} spectrum is slightly narrower in profile than the perturbation results, while the B_{2g} spectrum is wider. Although we have not tried to fit the self-consistent theory to the data on overdoped Bi 2212 in Fig. 5, it appears that if disorder is once again added, an equally good fit would be obtained using a slightly larger value of the coupling constant g_{eff} to offset the reduction due to self-consistency. We note, however, that the $z=2$ self-consistent

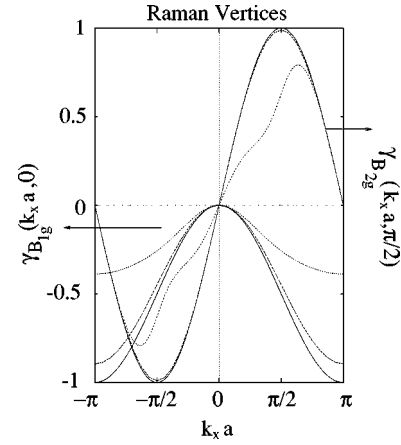


FIG. 8. Renormalization of the Raman vertices for the two symmetry channels evaluated for the lowest bosonic Matsubara frequency. The solid lines are the bare vertices, the dashed are the renormalized vertices for the $z=2$ (overdoped) parameters as in Fig. 3, and the dotted lines are the renormalized vertices corresponding to $z=1$ (underdoped) parameters, using $\alpha=16.7$ states/eV, corresponding to $\text{YBa}_2\text{Cu}_3\text{O}_{6.5}$ (Ref. 13).

treatment would not yield a particularly good fit to the data on optimally and underdoped systems, which show much more anisotropy than that indicated in Fig. 7.

This can be partially offset by interaction renormalization of the Raman vertex. When the vertex corrections are included, the B_{1g} spectrum is most affected, with an overall reduction intensity occurring over a wide region of frequencies, which we interpret as effects related to precursor SDW formation.¹³ This can be seen more clearly by examining the Raman vertices directly. In Fig. 8 we plot the B_{1g} and B_{2g} vertices for selected directions in the Brillouin zone for different values of the coupling g_{eff} and different scaling regimes. The $z=2$ curves correspond to the parameters used in Figs. 3 and 7, while the $z=1$ curves correspond to the values used for $\text{YBa}_2\text{Cu}_3\text{O}_{6.5}$ in Ref. 13, with $\alpha=16.7$ states/eV. Since $g=1$ eV and $t=250$ meV has been used for all curves, $g_{\text{eff}} = \alpha g^2/2t = 6.2(33.4)$ for the $z=2$ ($z=1$) curves in Fig. 8. We found no cases of symmetry mixing and the renormalized vertices retain their bare group transformation properties. Compared to the bare vertices, the B_{1g} vertex shows much more of reduction than the B_{2g} vertex. The renormalized vertex $\tilde{\gamma}$ for the B_{1g} channel is reduced in particular near the zone axes or “hot spots.” However, the B_{2g} vertex is hardly affected by the vertex renormalizations. This is consistent with the effects of a “cold” interaction probed along the zone diagonals. For $z=2$ the effects of the vertex corrections are small but increase dramatically for $z=1$. As the interaction is increased, the B_{1g} vertex is reduced dramatically near the “hot spots.” For $z=1$ the B_{1g} vertex is reduced by a factor 2 near the “hot spots” compared to its bare value, while the B_{2g} vertex is reduced by a smaller value 25%, and has a peak which is shifted out towards the “hot spots.” Since the Raman vertex renormalization enters with the opposite sign as the self-energy vertex correction, these results complement the results of Ref. 28 which showed that the effect of vertex corrections on the interaction yields an effectively increased coupling constant.

The vertex renormalization suppress the B_{1g} cross section

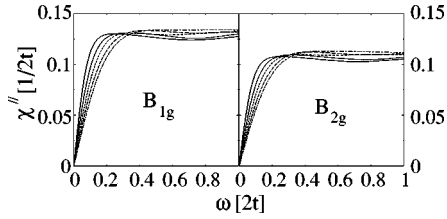


FIG. 9. The full Raman response for $z=1$ (underdoped) (evaluated with self-consistency and vertex renormalization) at temperatures $T/2t=0.03$ (solid), 0.04 (dotted), 0.5 (dashed), 0.6 (long-dashed), 0.7 (short-dashed), for the B_{1g} and B_{2g} channels. The parameters used corresponding to values for $\text{YBa}_2\text{Cu}_3\text{O}_{6.5}$ (Ref. 13).

compared to the B_{2g} cross section for larger interaction strengths. Since the B_{2g} vertex is affected less dramatically, the net effect would appear that the B_{2g} cross section remains relatively unchanged with increasing interaction, while the B_{1g} overall cross section comes down in magnitude to be closer to the B_{2g} value. We remark that this trend is consistent with the data from the cuprates which show a large decrease of the B_{1g} to B_{2g} ratio of the Raman spectra upon underdoping⁷ which we relate to the growth of ‘‘hot spots’’ intensity and subsequently large vertex renormalizations.

This can be seen more clearly in Fig. 9, which shows the full Raman response for larger values of the coupling g_{eff} corresponding to $\text{YBa}_2\text{Cu}_3\text{O}_{6.5}$.¹³ The spectra are much flatter than those calculated for smaller coupling constants, and appear to differ only quantitatively. The effect of the anisotropy of the scattering rate appears to have been washed out due to self-consistency, as the spectra have a ‘‘shoulder’’ at the same frequency and show roughly the same temperature dependence. However, the overall magnitude of the spectra at larger frequency shifts is reduced for the B_{1g} spectra relative to the B_{2g} spectra, leading to a ratio of the continua nearly equal to 1. As indicated in Fig. 8, this is entirely due to the vertex renormalization. While the relative magnitude of the continua and overall line shape is similar to that seen in experiments at a single temperature,⁷ the temperature dependence seen in experiments is qualitatively different.

This can be explored in more detail by plotting in Fig. 10 the inverse slope of the Raman spectra for the self-consistent and vertex corrected calculation. These results are qualitatively different from the perturbative treatment as discussed earlier. From Eq. (15) the inverse Raman slope has the same behavior as the QP scattering rate at zero frequency. If no disorder is included then the inverse Raman slope varies as T^2 below a characteristic T^* and crosses over to T at larger temperatures. T^* is connected with ω_{sf} , and is generally dependent on parameter choices. However Fig. 10 shows that the vertex corrected, self-consistent treatment does not show similar behavior. For the $z=2$ scaling regime, the inverse slope is proportional to T down to the lowest temperatures reachable for our level of numerical accuracy, while for the $z=1$ regime, the inverse slope appears to extrapolate to a nonzero value at $T=0$. This is also seen in FLEX calculations.¹¹ A simple connection between these and the perturbative results is that the self-consistency leads to a strong downward renormalization of ω_{sf} and a much lower crossover T^* to Fermi-liquid-like behavior. The renormal-

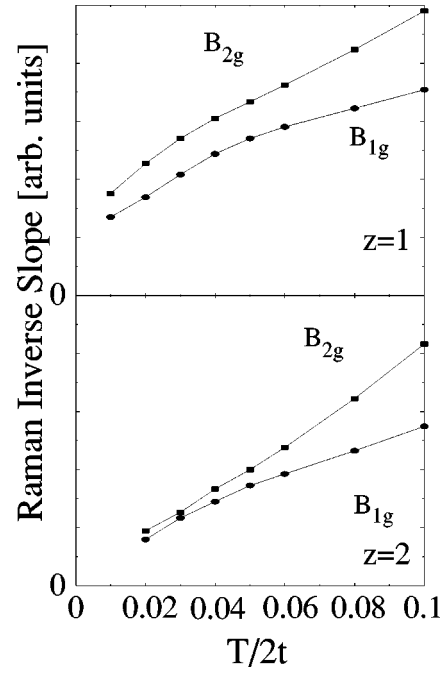


FIG. 10. The temperature dependence of the Raman inverse slope calculated self-consistently with vertex corrections evaluated for both symmetries and scaling regimes.

ization is stronger for the $z=1$ case than $z=2$, in agreement with our earlier discussion. Our results thus indicate that the inverse slope should fall as T is decreased until $\sim T_{\text{cr}}$ which separates the $z=1$ and $z=2$ scaling behavior, at which point the slope should become less T dependent. Such behavior has been reported by Naeini *et al.* in slightly overdoped $\text{La}_{1-x}\text{Sr}_x\text{CuO}_4$ (Ref. 23) and agrees well with the NAFI results.

While this behavior is similar to what has been observed in the B_{2g} channel, the theory does not predict a considerable difference for the B_{1g} channel. From our calculations, it appears that the effect of self-consistency obscures the anisotropy inherent in the model, leading to a temperature-dependent behavior which is similar for both channels. While the effect of vertex corrections appears to heighten the anisotropy, as shown in Fig. 8, the self-consistency appears to dominate the response, as seen in Fig. 10. It would appear then that a treatment which neglected self-consistency and focused only on vertex renormalizations would lead to a more apt description of the experiments. This remains to be explored.

VI. SUMMARY AND CONCLUSIONS

In summary we have seen how anisotropic QP scattering leads to manifestly channel-dependent Raman cross sections and how through a careful examination of the temperature dependence of the spectra, important information can be extracted concerning anisotropic QP dynamics. The coherence or incoherence of the QP’s spectral function can be probed directly via Raman scattering, thereby offering an additional avenue besides ARPES to explore momentum resolved QP information. Signatures of a strong interaction are (1) the position of a weak peak in the spectrum occurring at large frequency shifts, (2) the increased overall magnitude of the

spectra, and (3) anomalous temperature dependence of the spectra. If the interaction is strongly anisotropic, these features are different for different polarization channels. The QP dynamics can be probed by examining the temperature dependence of both the low and high frequency portions of the channel-dependent Raman response. For the cuprates, the consequence of an interaction which scatters QP's with relative momentum of the antiferromagnetic lattice vector \mathbf{Q} are (1) a stronger overall signal, (2) a peak at higher frequencies, and (3) a weaker temperature dependence of the slope of the response in the B_{1g} channel compared to the B_{2g} channel.

Excellent agreement of the NAFL model was found with the Raman results on overdoped Bi 2212 [and La 214 (Ref. 23)]. With the inclusion of impurity scattering, the Raman response calculated in a perturbative way in NAFL yields a correct description of the spectra at a variety of temperatures. Improvements to the theory can be made with more accurate determination of the parameters of the theory via other experimental probes.

The effect of a more self-consistent treatment leads to an overall reduction of anisotropy effects and a more isotropic Raman response, in contradiction to the experiments on optimally and underdoped cuprates, at least for the B_{1g} channel. The self-consistency yields a much weaker Fermi-liquid-like behavior than that obtained via a perturbative approach. However, the theory does not adequately describe the larger relatively incoherent scattering probed by the B_{1g} light orientations. Improvements can be made by once again exploring different parameter choices, but the nearly temperature independence of the B_{1g} response seen in the cuprates must be obtained by tuning both ω_{sf} and ξ to have a strongly increasing interaction peaked near (π, π) transfers to offset

the loss of phase space for QP scattering as the temperature is lowered. This remains to be explored.

Interestingly, the role of vertex corrections may help to obtain such a behavior. For larger couplings, the vertex corrections were found to be particularly large near the "hot spots" and led to a subsequently reduced vertex and overall signal for B_{1g} polarizations. Only a small change was seen for the B_{2g} channel. This general behavior has been observed in Y 123 and La 214, and has been attributed to the opening of a pseudogap. More than likely it would be important to also employ vertex corrections to the self-energy and to go beyond the simple calculations as performed here. Diagrammatically we have evaluated the lowest order diagrams for the self-energy, and we include the interactions in the Raman response through uncrossed vertex corrections (ladder approximation). We do not expect that these calculations can describe very strong spin fluctuations, but our approach in principle should give us an insight as to what is the most important physics we might expect as the strength of the spin fluctuations is increased by removing oxygen. This remains an open challenge.

ACKNOWLEDGMENTS

The authors would like to thank M. Opel, R. Nemetschek, and R. Hackl for making the data presented in Fig. 5 available to us prior to publication. T.P.D. would like to acknowledge helpful conversations with D. Pines, J. Schmalian, and B. Stojković. Acknowledgment (T.P.D.) is made to the Donors of the Petroleum Research Fund, administered by the American Chemical Society, for partial support of this research.

-
- ¹D.S. Marshall, D. S. Dessau, A. G. Loeser, C.-H. Park, A. Y. Matsuura, J. N. Eckstein, I. Bozovic, P. Fournier, A. Kapitulnik, W. E. Spicer, and Z.-X. Shen, *Phys. Rev. Lett.* **76**, 4841 (1996).
- ²A. G. Loeser, Z.-X. Shen, D. S. Dessau, D. S. Marshall, C. H. Park, P. Fournier, and A. Kapitulnik, *Science* **273**, 325 (1996); H. Ding, M. R. Norman, T. Yokoya, T. Takeuchi, M. Randeria, J. C. Campuzano, T. Takahashi, T. Mochiku, and K. Kadowaki, *Phys. Rev. Lett.* **78**, 2628 (1997).
- ³T. P. Devereaux, D. Einzel, B. Stadlober, R. Hackl, D. H. Leach, and J. J. Neumeier, *Phys. Rev. Lett.* **72**, 396 (1994); for a recent review, see T. P. Devereaux and A. P. Kampf, *Int. J. Mod. Phys. B* **11**, 2093 (1997).
- ⁴G. Blumberg, P. Abbamonte, M. V. Klein, W. C. Lee, D. M. Ginsberg, L. L. Miller, and A. Zibold, *Phys. Rev. B* **53**, R11 930 (1996); D. Einzel and R. Hackl, *J. Raman Spectrosc.* **27**, 307 (1996); D. Reznik, S. L. Cooper, M. V. Klein, W. C. Lee, D. M. Ginsberg, A. A. Maksimov, A. V. Puchkov, I. I. Tartakovskii, and S.-W. Cheong, *Phys. Rev. B* **48**, 7624 (1993).
- ⁵R. Hackl, M. Opel, P. F. Müller, G. Krug, B. Stadlober, R. Nemetschek, H. Berger, and L. Forró, *J. Low Temp. Phys.* **105**, 733 (1996).
- ⁶R. Hackl, G. Krug, R. Nemetschek, M. Opel, and B. Stadlober, *Proc. SPIE* **2696**, 194 (1996).
- ⁷X. K. Chen, J. G. Naeni, K. C. Hewitt, J. C. Irwin, R. Liang, and W. N. Hardy, *Phys. Rev. B* **56**, R513 (1997); R. Nemetschek, M. Opel, C. Hoffmann, P. F. Müller, R. Hackl, H. Berger, L. Forró, A. Erb, and E. Walker, *Phys. Rev. Lett.* **78**, 4837 (1997).
- ⁸A small temperature-dependent peak at 600 cm^{-1} in the B_{1g} channel has recently been observed [G. Blumberg, M. Kang, M. V. Klein, K. Kadowaki, and C. Kendziora, *Science* **278**, 1427 (1997)].
- ⁹L. B. Ioffe and A. J. Millis, *Phys. Rev. B* **58**, 11 631 (1998).
- ¹⁰Z.-X. Shen and J. R. Schrieffer, *Phys. Rev. Lett.* **78**, 1771 (1997).
- ¹¹J. Altmann, W. Brenig, and A. P. Kampf, cond-mat/9707267 (unpublished).
- ¹²A. Millis, H. Monien, and D. Pines, *Phys. Rev. B* **42**, 167 (1990).
- ¹³D. Pines, *Z. Phys. B* **103**, 129 (1997); A. V. Chubukov, D. Pines, and B. Stojković, *J. Phys.: Condens. Matter* **8**, 10 017 (1996); J. Schmalian, D. Pines, and B. Stojković, cond-mat/9804129, and references therein.
- ¹⁴D. Pines and B. Stojković, *Phys. Rev. B* **55**, 8576 (1997); **56**, 11 931 (1997).
- ¹⁵M. V. Klein and S. B. Dierker, *Phys. Rev. B* **29**, 4976 (1984); H. Monien and A. Zawadowski, *ibid.* **41**, 8798 (1990).
- ¹⁶J. Kosztin and A. Zawadowski, *Solid State Commun.* **78**, 1029 (1991).
- ¹⁷A. A. Abrikosov and V. M. Genkin, *Zh. Éksp. Teor. Fiz.* **40**, 842 (1973) [*Sov. Phys. JETP* **38**, 417 (1974)].
- ¹⁸P. Allen, *Phys. Rev. B* **13**, 1416 (1976).
- ¹⁹A. Zawadowski and A. Cardona, *Phys. Rev. B* **42**, 10 732 (1990).

- ²⁰A. Virosztek and J. Ruvalds, *Phys. Rev. B* **45**, 347 (1992).
- ²¹A. V. Chubukov, D. Pines, and B. P. Stojković, *J. Phys.: Condens. Matter* **8**, 10 017 (1996).
- ²²N. Bulut, D. Scalapino, and S. R. White, *J. Phys. Chem. Solids* **54**, 1109 (1993).
- ²³J. G. Naeini, X. K. Chen, K. C. Hewitt, J. C. Irwin, T. P. Devereaux, M. Okuya, T. Kimura, and K. Kishio, *Phys. Rev. B* **57**, R11 077 (1998).
- ²⁴C. Kendziora, M. C. Martin, J. Hartge, L. Mihaly, and L. Forró, *Phys. Rev. B* **48**, 3531 (1993).
- ²⁵M. Opel (private communication).
- ²⁶P. Monthoux and D. Pines, *Phys. Rev. B* **49**, 4261 (1994).
- ²⁷J. Vidberg and J. Serene, *J. Low Temp. Phys.* **29**, 179 (1977).
- ²⁸A. V. Chubukov, P. Monthoux, and D. Moor, *Phys. Rev. B* **56**, 7789 (1997); J. Schmalian (private communication).